Materials Advances

ROYAL SOCIETY OF CHEMISTRY

PAPER

View Article Online
View Journal | View Issue

Cite this: *Mater. Adv.*, 2025, 6, 6877

Comprehensive impedance spectroscopy, Raman, and infrared studies of the ferroelectric properties and application of $BiFeWO_6$

B. S. Tripathy,[a] Balaji Umapathi,[bc] Priyabrata Nayak[bc] and S. K. Parida *[a]

Tetragonal double perovskite $BiFeWO_6$ nanopowders were successfully synthesized *via* the solid-state reaction technique. Structural characterization using X-ray diffraction (XRD) revealed an average crystallite size of 11.6 nm with a lattice strain of 0.06499. The study of the microstructure of the sample reveals uniform distribution of well-grown grains and presence of all constituent elements in both weight and atomic percentages. Optical properties were investigated through ultraviolet (UV)-visible spectroscopy, which revealed a bandgap energy of 1.41 eV, highlighting its potential for photovoltaic applications. Raman spectroscopy confirmed the presence of all constituent elemental vibrational modes associated with various molecular bonding interactions in the studied material. Dielectric analysis exhibited a Maxwell–Wagner-type polarization effect, indicating its potential as a material with a high dielectric constant and low loss for energy storage devices. The study of impedance plots revealed a negative temperature coefficient of resistance (NTCR) behavior, whereas the electrical modulus study suggested the presence of a non-Debye-type relaxation mechanism. The study of AC conductivity *versus* frequency and temperature revealed the fact that the conduction mechanism is controlled by thermally activated charge carriers. Again, semicircular Nyquist and Cole–Cole plots confirmed the semiconductor nature and well-supported impedance results. The resistance *versus* temperature plot showed an NTC thermistor character, indicating that $BiFeWO_6$ is a strong candidate for temperature sensor devices.

Received 13th June 2025,
Accepted 10th August 2025

DOI: 10.1039/d5ma00643k

rsc.li/materials-advances

1. Introduction

The realization of multiferroic material systems has united scientists across the globe with a common interest in exploring the phenomena associated with it. The term multiferroic was coined by H. Schmid to define a material system having two or more primary ferroic properties (ferroelectricity, ferromagnetism, ferroelasticity, and pyroelectric) in a single phase.[1,2] The term magnetoelectric is a sub-group of multiferroic systems that includes materials in which electric polarisation can be controlled by varying magnetic fields and *vice versa*. These materials are characterized by electromagnetic coupling. However, the definition included all the coupling mechanisms associated with charge and spin degrees of freedom.[3,4] Around the 1950s, when ferroelectricity and anti-ferromagnetism were very new physical phenomena, the Soviet Union was the first to try to combine ferroelectric order and magnetic order. Smolenski and Ioffe created magnetic long-range order while retaining the ferroelectric state in single crystals like $Pb(Fe_{0.5}Nb_{0.5})O_3$ and a polycrystalline solid solution like $(1-x)Pb(Fe_{0.66}W_{0.33})O_{3-x}$-$Pb(Mg_{0.5}W_{0.5})O_3$. By the 1960s, only 50 multiferroic systems were known, but none of them exhibited properties that were suitable for technological advancement.[5] In 1983, Baryakhtar *et al.* reported a model that elaborated on how magnetic order induces spontaneous electric polarization by breaking inversion symmetry. In 2000, Spaldin analyzed Ioffe's and Smolenski's work to explain the challenges in coexistence of ferroelectricity and ferromagetism in a perovskite. This helped scientists to understand the reason why attempts to devise a novel multiferroic failed and encouraged them to take the challenge to find new way to resolve the issue related to concurrence of ferroelectric and ferromagnetic. In this way, a new era of multiferroics began.[6]

Perovskites are multiferroic materials with the structural formula ABX_3, where A is a rare-earth or alkaline cation, B is a transition metal and X symbolizes a halide atom. BX_3 constitutes corner octahedra similar to ReO_3, and A occupies the body center position with coordination number 12. Perovskite oxides

[a] *Department of Physics, ITER, Siksha O Anusandhan Deemed to be University, Bhubaneswar, India. E-mail: santoshparida@soa.ac.in*
[b] *Pyrometallurgy & Materials Engineering Department, CSIR-IMMT, Bhubaneswar, India*
[c] *Academy of Scientific and Innovative Research, Ghaziabad, India*

have different kinds of electronic properties. $BaTiO_3$ is ferroelectric, $SrRuO_3$ is ferromagnetic, $LaFeO_3$ is weakly ferromagnetic, and $BaPb_{1-x}Bi_xO_3$ shows superconducting behavior. By contrast, $LaCoO_3$ shows the insulator-metal transition at the same time that many perovskites have metallic conductivity, *e.g.*, ReO_3, A_xWO_3, $LaTiO_3$, $SrVO_3$ & $LaNiO_3$. Interestingly, the strong cation–anion–cation interaction is the cause of metallic conductivity in the ceramic compounds. To enhance the properties in the single perovskite, the doubling of the unit cell to create a material called the double perovskite was introduced.

These materials are invented by doping suitable elements at A and B sites, having general structural formula $A'A''B'B''O_6$ or $A_2B'B''O_6$. Suitable elements for B site doping include the 3d/4d/5d transition metals and the lanthanide series with small ionic radii. These elements comprise the largest proportion in the periodic table, thus providing a wide range of choices for scientists to tailor the material properties for potential applications. A site can also host two different cations as in $A'A''B'B''O_6$, which is named as the double–double perovskite. Double perovskites are suitable candidates for replacing single perovskites to attain better performance and stability. Specifically, they have a greater space to accommodate additional atoms; hence, increasing the compositional space of the perovskite family. Another advantage is the complex atomic environment that is created by double perovskites, resulting in electronic structures that are absent in single perovskites. These perovskites are chemically stable under catalytic conditions that include a wide range of oxidizing and reducing agents, acidic or basic solutions, humidity, heat, light, and CO_2 environments. However, the lead toxicity raises a major concern about the commercialization and large-scale application of halide perovskites. Exposure to a small quantity can cause severe damage to the nervous system and renal system, as well as impaired bone calcification. Lead halides having high solubility product constant (K_{SP}) values are easily soluble in water, causing damage to ecosystems in the environment. Therefore, scientists are currently searching for good alternatives to replace lead for the manufacture of perovskites with low toxicity and high performance.[7] Ravi Shankar *et al.* found a long-range anti-ferromagnetic ordering and magnetoelectric coupling in $NaLnNiWO_6$ (Ln = Er, Tm, Lu).[8] Other materials include Na_3AlF_6, which is a very important material for aluminum processing, and Sr_2FeMoO_6, which is of greater importance due to its unusual electric and magnetic properties arising from the alternation between Mo^V and Fe^{III} ions.[9] L. Boudad *et al.* reported on the cubic double perovskites $EuBaFeTiO_6$ and $LaBaFeTiO_6$ with large band gap values of 3.53 eV and 3.75 eV, respectively.[10] Rutuparna Das *et al.* reported on the anti-ferromagnetic ordering in Y_2CoMnO_6.[11] Liangdong Chen *et al.* reported on the application of the double perovskite as oxygen evolution reaction electrocatalysts and supercapacitors.[12]

Ferrite ferromagnetic oxides are known to have high resistivity, as well as high permeability. Although ferromagnetic alloys have more than double the value of saturation polarization compared to ferrites, ferrites have advantages in terms of their applicability at higher frequency, higher resistivity, low cost, high heat, and corrosion resistance.[13–15] There is a growing interest in the synthesis of ferrites because of their chemical stability, biological compatibility, relative ease of preparation, and numerous applications associated with ferrites, including mechanical applications,[16] magnetic data storage, microwave absorbers,[17–19] sealants, lubricants, and coolants.[20,21] The main reason for the increased applicability of ferrites is the ease of detection and manipulation of the application of an external magnetic field. Lithium ferrite, due to its high Curie temperature (T_c) and high saturation magnetization (M_s), low magnetic losses, high chemical stability, and high resistivity, is a magnetic material with high technological and scientific interests.[22–24]

Bismuth ferrite (BFO) is a multiferroic material that exhibits both ferromagnetic and ferroelectric properties. It is also known for its high transition temperatures ($T_c \sim 1100$ K, $T_N \sim 653$ K). Experimental results on BFO were first reported in 1957.[24–26] Later, its room-temperature ferroelectric property with remnant polarization (P_r) was reported to be more than 50 mC cm^{-2} in 1970. Interestingly, research interest in BFO surged in 2003 when Ramesh *et al.* reported on an exceptional increase in the remanent polarization (P_r), reaching 60 μC cm^{-2}, approximately 15 times higher than that previously recorded in bulk BFO samples. This breakthrough has since driven further advancements in the material's structural and electronic properties, solidifying its potential in next-generation magnetoelectric devices.[26–28] In recent times, numerous $BiFeO_3$-based multiferroics have been developed by doping suitable elements at either the A-site or B-site or both, which has led to a better understanding of the underlying magnetic and electric mechanisms. These $BiFeO_3$-based multiferroics are thus a promising candidate for applications in next-generation storage, information, and spintronics. In traditional ferroelectric materials, the transition metals are characterized by an empty d-shell, known as a d^0 configuration. However, the BFO ceramic is different as it does not have any transition metal with an empty d-shell. Instead, it contains Fe^{3+} ions with a d^5 configuration. Interestingly, the ferroelectricity in BFO is not due to these transition metal ions. It is caused by the Bi^{3+} ions (A site cation). An active lone pair of electrons in the valence state in Bi^{3+} ions in the sp^2 hybridized states take part in chemical bonding. The presence of the (s^2) lone pair electrons in the Bi ions leads to a disruption of the local inversion symmetry in BFO. Consequently, the small B-site cation, Fe, minimizes its energy by shifting along the [111] crystallographic directions, influencing the material's structural and electronic properties. This is a unique characteristic of BFO that sets it apart from conventional ferroelectric materials.[29]

Tungsten trioxide (WO_3) is indeed a fascinating compound, where its structure is temperature-dependent. It is tetragonal at temperatures above 740 °C, orthorhombic from 330 to 740 °C, monoclinic from 17 to 330 °C, triclinic from −50 to 17 °C, and monoclinic again at temperatures below −50 °C. The most common structure of WO_3 is monoclinic with the space group $P21/n$. The pure compound is an electric insulator, but oxygen-deficient varieties, such as $WO_{2.90} = W_{20}O_{58}$, are dark blue to

purple and conduct electricity. These can be prepared by combining the trioxide and the dioxide WO_2 at 1000 °C in a vacuum. Tungsten trioxide is a transition metal oxide known for its n-type semiconductor properties, exhibiting a bandgap ranging from 2.6 to 3.0 eV. This material has garnered significant interest due to its high coloration efficiency, remarkable chemical stability, rapid switching kinetics, and excellent electrochemical activity. These characteristics make WO_3 a promising candidate for applications in electrochromic devices, gas sensors, and energy storage systems.[30]

Lastly, WO_3 exhibits fascinating characteristics such as structural and ferroelectric properties, among others. The manifestation of these properties is influenced by the synthesis method employed and the specific conditions under which the experiments are conducted. Notably, WO_3 displays ferroelectric properties at low temperatures (below 230 K).[31] Consequently, it is anticipated that incorporating a minor quantity of this compound into BFO could lead to intriguing multiferroic properties, including a transition temperature shift. A similar type of work on modified $BiFeWO_6$ has already been reported in the literature.[32–35] Interestingly, in this context, the preliminary structural analysis, microstructure, dielectric, electrical, Raman, infrared, and ferroelectric properties of $BiFeWO_6$ ceramics with potential applications have not explored in a single investigation. Therefore, the authors have decided to synthesize the same $BiFeWO_6$ ceramic in the solid-state reaction method and investigate all of the mentioned physical properties in one frame, searching for possible applications in the field of science and technology. Finally, a comprehensive study on lead-free compound $BiFeWO_6$ is discussed extensively in the next section.

2. Experimental details

2.1. Raw materials

A cost-effective standard fabrication technique, the high-temperature sintering method, was employed to synthesize the single-phase polycrystalline double perovskite $BiFeWO_6$. Analytical reagent (AR) grade raw materials, including Bi_2O_3 (Bismuth oxide), WO_3 (Tungsten oxide), and $Fe_{20}O_3$ (Iron(III) oxide), were sourced from M/S Hi-Media Lab with a purity of $\geq$99%. The raw materials were precisely weighed in stoichiometric ratios using an electronic balance [New Classic MF: MODEL-ML204/A01], ensuring an accuracy of up to four decimal places. The sample preparation followed the chemical equation detailed below.

$$0.5Bi_2O_3 + 0.5Fe_2O_3 + WO_3 \rightarrow BiFeWO_6$$

2.2. Synthesis and sintering

The weighed samples were thoroughly mixed through dry grinding using an agate mortar and pestle for 4 h for uniform mixing and reduction of the powder sample into the nanoscale. The prepared mixture was subjected to calcination in a high-purity alumina crucible for six hours using a high-temperature muffle furnace at 850 °C to ensure phase stability. The formation of a stable sample was verified through X-ray diffraction (XRD) analysis using a Rigaku Japan Ultima IV diffractometer (Cu Kα, λ = 1.540510 Å). The diffraction patterns were recorded over a broad range of Bragg angles ($20^\circ \leq \theta \leq 80^\circ$) at a scanning speed of 0.2° min^{-1} to confirm crystallinity and phase purity. Polyvinyl alcohol was added to the calcined powder in 1 wt% to make cylindrical pellets using a KBr hydraulic press under a pressure of 4×10^6 N m^{-2} of 1–2 mm thickness and 10–12 mm diameter. The pellet undergoes sintering at 800 °C for three hours to enhance its compactness and density, ensuring improved structural integrity and material stability.

2.3. Characterization

The structural characterization was carried out using an X-ray diffractometer (Rigaku Japan Ultima IV, Cu Kα, λ = 1.540510 Å) to determine the crystallinity and phase purity. Microstructural analysis was conducted using scanning electron microscopy (SEM), with data obtained through an SEM-EDX system (Model Zeiss EVO 18) to examine the surface morphology and elemental composition. The optical properties of the synthesized sample were evaluated using a UV spectrometer (CECIL CE3055, 3000 series), providing insights into its absorption and bandgap characteristics. Additionally, the dielectric properties were investigated using an impedance analyzer, enabling the assessment of its electrical behavior and potential applications in electronic devices. Micro-Raman spectroscopy [lab Ram HR800, Jobin Yvon, wavelength = 488 nm] was tailored to record the characteristic vibrational modes of the prepared sample. High-temperature dielectric data were recorded from the LCR analyzer MODEL: N4L PSM, 1735 provided with a frequency range of 1 kHz–1 MHz and temperature range of 25–500 °C. The ferroelectric nature of the prepared sample was tested by the polarization *versus* electric field (*P*–*E*) loop tracer (M/S Marine, India), and different possibilities for the device applications were explored.

3. Results and discussions

3.1. Sample formation

Goldschmidt's tolerance factor, introduced in 1926, plays a crucial role in predicting the formation, crystal symmetry, and structural stability of the material BMFW. It provides a mathematical framework for assessing the ionic radii compatibility of the constituent elements, ensuring optimal lattice stability and phase formation. This factor can be expressed as:

$$t = \frac{r_{(A+A')} + r_{(O)}}{\sqrt{2}\left(r_{(B+B')/2} + r_O\right)}$$

where RA, $r_{A'}$, r_B, $r_{B'}$, and r_O represent the ionic radii of the A-site cation, A′-site cation, B-site cation, B′-site cation, and the oxygen anion, respectively. The tolerance factor of the studied material has been calculated as 0.96, suggesting a tetragonal structural symmetry.[36]

3.2. XRD analysis

X-ray diffraction (XRD) is a crucial analytical technique for examining the crystalline structure of ceramic materials. By analyzing the angles and intensities of diffracted X-rays, XRD provides essential information about the crystal lattice, phase composition, and crystallite size of ceramics.

Fig. 1(a) show the X-ray diffraction pattern of the $BiFeWO_6$ ceramic at room temperature. The structural analysis was done using X-Pert High-Score software and a tetragonal structure was obtained for $BiFeWO_6$ (JCPDS: 00-038-1289). The structural lattice parameters are as follows: $a = b = 12.4400$ Å, $c = 3.6400$ Å and $\alpha = \beta = \gamma = 90^\circ$. The average crystallite size (D) and lattice strain (ε) were determined using Williamson–Hall (W–H) plot, as shown in Fig. 1(b). The mathematical relation of the W–H method can be written as $\beta\cos\theta = 4\varepsilon\sin\theta + \frac{k\lambda}{D}$, where β represents the full width at half-maximum (FWHM) of the reflection, θ is the Bragg angle, λ denotes the X-ray wavelength ($\sim$0.154 nm), and k is a dimensionless shape factor, typically assigned a value of $\sim$0.89. The calculated average crystallite size was found to be 11.69 nm, with dislocation density $\sigma = \frac{1}{D^2} = 7.3 \times 10^{-3}\ \mathrm{nm}^{-2}$ and lattice micro-strain of 0.06499.

3.3. Microstructural analysis

Scanning electron microscopy (SEM) utilizes probing beams that are narrower at both low and high electron energy, enhancing spatial resolution while reducing sample damage. It enables the identification of contamination spots in small areas at electron-accelerating voltages and is compatible with energy-dispersive X-ray spectroscopy. It also allows the application of low kinetic energy electrons closer to the immediate material surface and eliminates the need for conducting coatings on insulating materials.[37] Fig. 2(a) shows the SEM micrograph of the studied sample. The figure shows the presence of irregularly shaped grains with non-uniform size, showing that the polycrystalline sample is distorted. However, the grains are distributed uniformly with well-defined grain boundaries, which can be seen from the figure. The high density of the formed sample is confirmed by the closely packed grains leaving negligible voids.

Fig. 2(b) displays the grain distribution curve, with the grain size (in μm) on the x-axis and the number of particles on the y-axis. ImageJ software was utilized to determine the number of particles and their corresponding grain sizes. The average grain size, determined by fitting the histogram data, was found to be 0.818 μm. Grains are highly compact and provide well-defined grain boundaries. The agglomeration ratio, *i.e.*, ratio of the grain size to crystallite size, is found to be 70, which may be one of the reasons for the better electrical conduction process.[38] Fig. 2(c) shows the EDX spectrum of the $BiFeWO_6$ ceramic at room temperature. It is observed that all the constituents (Bi, Fe, W, O) are present in both weight and atomic percentages.

3.4. UV-Visible spectroscopy

UV-visible spectroscopy is often used to provide characterization data for various materials including both organic and inorganic chemical substances. When an electronic transition is induced in a molecule or ion due to the radiation, the material exhibits absorption in the visible or ultra-violet (UV) region. As a result, a change in electronic structure occurs in the material due to the absorption of light in the visible or UV region. Functional groups in inorganic or organic, solid, or liquid materials can be observed using UV-visible spectroscopy. Depending on the degree of transmittance or absorbance of radiation and sample behavior, UV-visible spectroscopy provides details regarding the bandgap measurements.[39]

Fig. 3(a) [inset] shows the absorbance spectrum in the wavelength range of 200–1100 nm. The sample shows an absorbance peak at 305 nm which is in the UV range; however, the sample absorbs all the visible radiations. Bi-based oxide materials can make use of valence bands O 2p and Bi 6s, have a low bandgap, and absorb more visible radiation.[15,16,40]

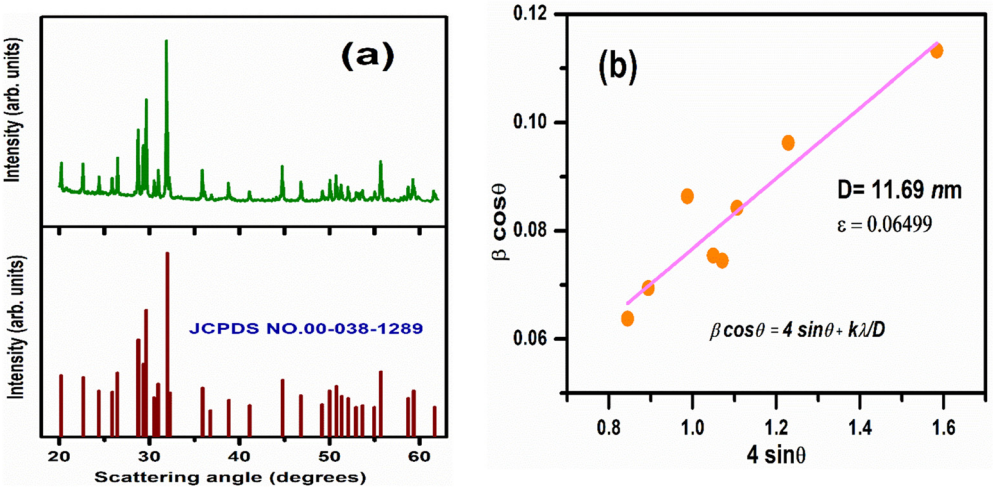

Fig. 1 (a) XRD pattern and (b) W–H plots of the BFWO ceramic.

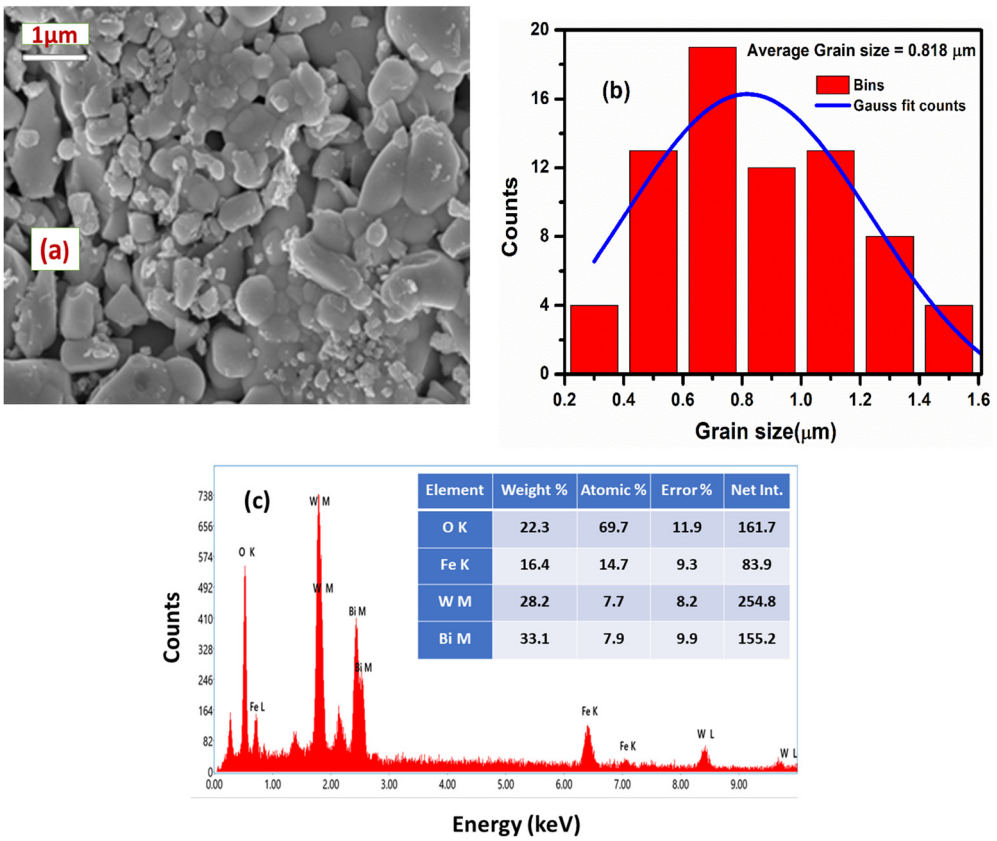

Fig. 2 (a) SEM micrograph, (b) Gaussian fitting grain size using ImageJ software, and (c) EDX spectrum confirming the presence of all constituent elements.

The bandgaps in semiconducting materials can be either a directly allowed, indirectly allowed, directly forbidden, or indirectly forbidden transition depending on the type of material.

In the case of a directly (vertical) allowed transition, the energy-dependent absorption coefficient $\alpha(E)$ follows:

$$\alpha_{\mathrm{dir}}\,(E < E_{\mathrm{g}}) = 0$$

and

$$\alpha_{\mathrm{dir}}\,(E \geq E_{\mathrm{g}}) \propto (E - E_{\mathrm{g}})^{1/2}$$

where α_{dir} is the direct optical absorption coefficient, $E = h\nu$ (photon energy), and E_{g} is the band gap energy. Such behavior is expected for transitions with negligible changes in the electron wave vector k with factors regarding the atomic bonding and selection rules. In such a case, the E_{g} value can be calculated by extrapolating the linear least squares fit α^2 to 0 in the "α^2 *versus* E_{g} plot". In contrast, the indirect transition or non-vertical optical transition involves a photon and at least one phonon to satisfy a conservation of momentum. The transition rate taking place in the case of indirect optical band gap semiconductors is smaller than that in the case of direct band gap semiconductors. The corresponding $\alpha(E)$ follows the relation:

$$\alpha_{\mathrm{dir}}\,(E < E_{\mathrm{g}}) = 0$$

and

$$\alpha_{\mathrm{dir}}\,(E \geq E_{\mathrm{g}}) \propto (E \pm h\nu - E_{\mathrm{g}})^{1/2},$$

where $h\nu$ represents the energy of the phonon, $+h\nu$ represents the energy of the emitted phonon, and $-h\nu$ is the energy of the absorbed phonon. In most cases, the contribution of $h\nu$ can be neglected.

The indirect E_{g} can be calculated by extrapolating the linear least squares fit of $\alpha^{1/2}$ to zero "$\alpha^{1/2}$ *versus* E" plot, as shown in Fig. 3(b). The optical bandgap of the $BiFeWO_6$ sample is calculated following Tauc's mathematical formulation; $\alpha h\nu = A(h\nu - E_{\mathrm{g}})^{\gamma}$, where A denotes the characteristic parameter, and n represents the exponential term.[41] The parameter γ takes values of 1/2, 2, 3/2, and 3, corresponding to directly allowed, indirectly allowed, directly forbidden, and indirectly forbidden band transitions, respectively.[42] The value of the indirect bandgap energy E_{g} = 1.41 eV in the sample is calculated by extrapolating the linear portion of the plot onto the X-axis, corresponding to energy with $(\alpha h\nu)^{1/2} = 0$. The calculated bandgap value for $BiFeWO_6$ is lower than those from earlier reported articles (2.24 eV,[43] 1.70 eV,[44] 1.65[45]).

The decrease in the bandgap value is due to the oxygen vacancies, which results in positive structural defects. Such sites can capture one or two electrons and act as donor centres.

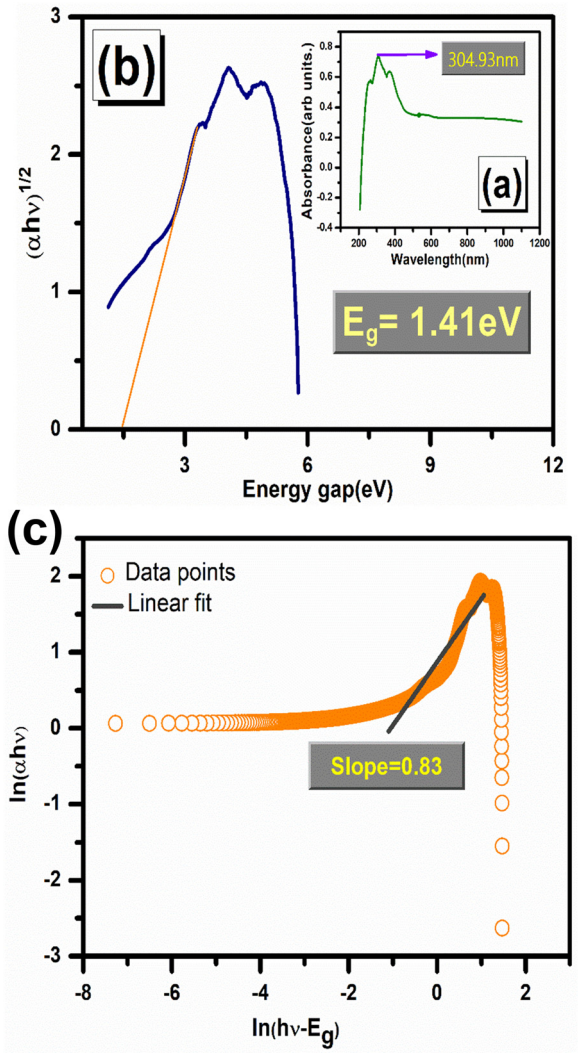

Fig. 3 (a) Absorbance spectrum [inset] and (b) Tauc plot of $BiFeWO_6$. (c) Calculation of the n value from $\ln(\alpha h\nu)$ *versus* $\ln(h\nu - E_g)$ of $BiFeWO_6$.

These donor centre levels are located close to the valence band.[38] Tauc's formulation can also be written as: $\ln(\alpha h\nu) = \ln A + \gamma \ln(h\nu - E_g)$. The value of n is determined from the slope of the plot of $\ln(\alpha h\nu)$ *versus* $\ln(h\nu - E_g)$. The calculated slope of 0.83 deviates from the expected value of 0.5, which corresponds to a direct bandgap transition. This deviation confirms that the sample exhibits an indirect electronic transition.[46]

The refractive index (n) is an important optical constant that depends on the wavelength of electromagnetic radiation through dispersion, and helps in understanding the optical device application potentiality of any prepared material.[47] The band gap decreases with an increase in the refractive index in a semiconducting material, which tells us that these two quantities must be related. S. K. Tripathy *et al.* proposed a relation between the refractive index and energy band gap, $n = n_o(1 + \alpha e^{-\beta E})$, where n_o, α and β are the constants with values of 1.73, 1.9017 and 0.539 $(eV)^{-1}$, respectively. Using this formulation, the value of the refractive index for the sample was found to be 3.27.[48] The refractive index value can be calculated by a model proposed by Kumar and Singh as it includes many different materials, including semiconductors materials, halides, and insulators. As per the model, the value of the refractive index can be calculated using $n = KE_g^C$, where K = 3.3668 and C = −0.32234 are constants.[24,25] So, from the mathematical formulation, the η value was found to be 3.014. The electron polarizability (α') can be calculated by using the formula, $\alpha' = \left[\frac{12.41 - 3\sqrt{E_g - 0.365}}{12.41}\right]\frac{M}{\rho} \times 0.395 \times 10^{-24}$ cm^3, where M is the molecular weight (in g mol^{-1}) and ρ is the density of the material (in g cm^{-3}).[49] Following the formulation, the value of the electron polarizability (α') is found to be 24.84 × 10^{-24} cm^3. χ^3 is the third-order non-linear optical susceptibility and provides detailed information about the strength of chemical bonds between molecules in the synthesized nanocrystalline materials. This quantity can be calculated from the first-order susceptibility (χ^1) of ceramics by using $\chi^1 = \frac{n^2 - 1}{4\pi}$ and $\chi^3 = A[\chi^1]^4$, where the value of $A = 1.7 \times 10^{-10}$ esu. Using the above formulae, the values of the first-order and third-order susceptibility was found to be 0.77 and 6.03 × 10^{-11} esu, respectively.[27,28] Another important parameter is the carrier concentration (n_c) in the field of photovoltaics, as it influences the doping and the oxidation states of the crystals.[50] The relation between the calculated bandgap (E_g) and carrier concentration (n_c) can be stated as $n_c = \left[\frac{E_g}{2.7924462} \times 10^{37}\right]^{3/2}$,[51] which gives the value of n_c as 1.14 × 10^{55}. This makes the material a suitable and potential candidate for optoelectronic applications. We have also calculated the high-frequency dielectric constant (ε_∞) and static dielectric constant (ε_0) using the following mathematical formulation: $\varepsilon_\infty = n^2$ and $\varepsilon_\infty = 11.26–1.42E_g$ and $\varepsilon_\infty = 18.52–3.08E_g$.[52] The values of the high-frequency dielectric constant were calculated to be 10.69 (from the refractive index) and 9.2578 (from the energy band gap), and the static dielectric constant value for the prepared sample was found to be 14.177. The oscillator strength value was found to be 2.82 eV for the prepared sample, calculated using the following relation: oscillator strength = $2E_g$.[49,53] The results of different parameters tell us the potentiality of the sample for application in optoelectronic devices. The absorption peak occurs at the UV region of the radiation, which indicates the material's UV sensing application.

3.5. Raman study

Raman spectroscopy is a powerful analytical technique used to study the vibrational, rotational, and other low-frequency modes in molecules. It is based on the inelastic scattering of light, where incident photons interact with molecular vibrations, leading to a shift in their energy. This technique is widely used in material science, chemistry, biology, and nanotechnology for identifying molecular compositions and structural changes. Raman spectroscopy is highly sensitive to molecular fingerprints, making it essential for non-destructive chemical analysis. It plays a crucial role in studying crystal structures, phase transitions, and even biomedical diagnostics. Its ability to analyze substances without extensive sample

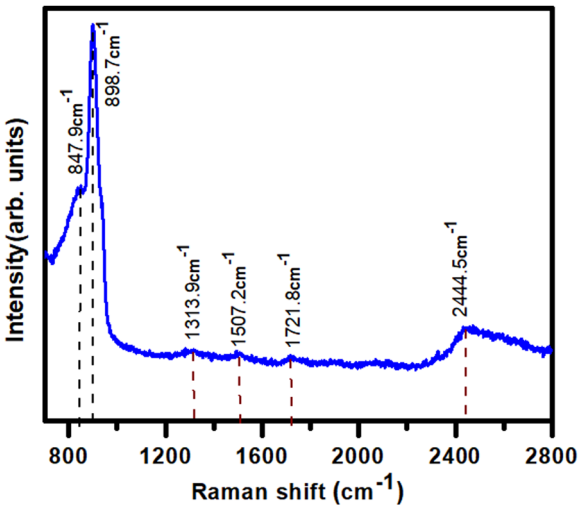

Fig. 4 Raman spectrum of $BiFeWO_6$.

preparation makes it invaluable in scientific and industrial applications.

Fig. 4 shows the Raman spectrum of the $BiFeWO_6$ ceramic at room temperature. The spectrum reveals distinct peaks at 847.9 cm^{-1}, 898.756 cm^{-1}, 1313.997 cm^{-1}, 1507.154 cm^{-1}, 1721.773 cm^{-1}, and 2444.479 cm^{-1}. These spectral features were compared with the existing literature to determine their molecular origins. A study of the Raman spectra from previously published works suggests that the 847.9 cm^{-1} & 898.756 cm^{-1} peaks correspond to the Fe–O or W–O stretching vibrations,[54] indicating the interaction between iron & tungsten with oxygen; the 1313.997 cm^{-1} & 1507.154 cm^{-1} peaks are likely associated with Bi–O or Fe–O bond interactions[55]; and the 1721.773 cm^{-1} & 2444.479 cm^{-1} peaks may be linked to higher-order phonon modes or lattice strain.[56]

3.6. Dielectric study

Fig. 5(a and b) illustrates the variation of the dielectric constant (ε_r) and dielectric loss ($\tan\delta$) as a function of frequency in the range of 1 kHz to 1 MHz and temperature range of 25 °C to 500 °C. From Fig. 5(a), we can see that the dielectric values in the low-frequency region are very high in magnitude and dispersed, and increase with the temperature rise. However, the value of the dielectric constant decreases with the rise in frequency of the applied external electric field, and assumes a minimum value at 1 MHz even at very high temperatures. The dielectric constant value is determined by the ability of the dipolar orientation w.r.t. the applied external field. The types of polarization occurring are classified into four types: electronic,

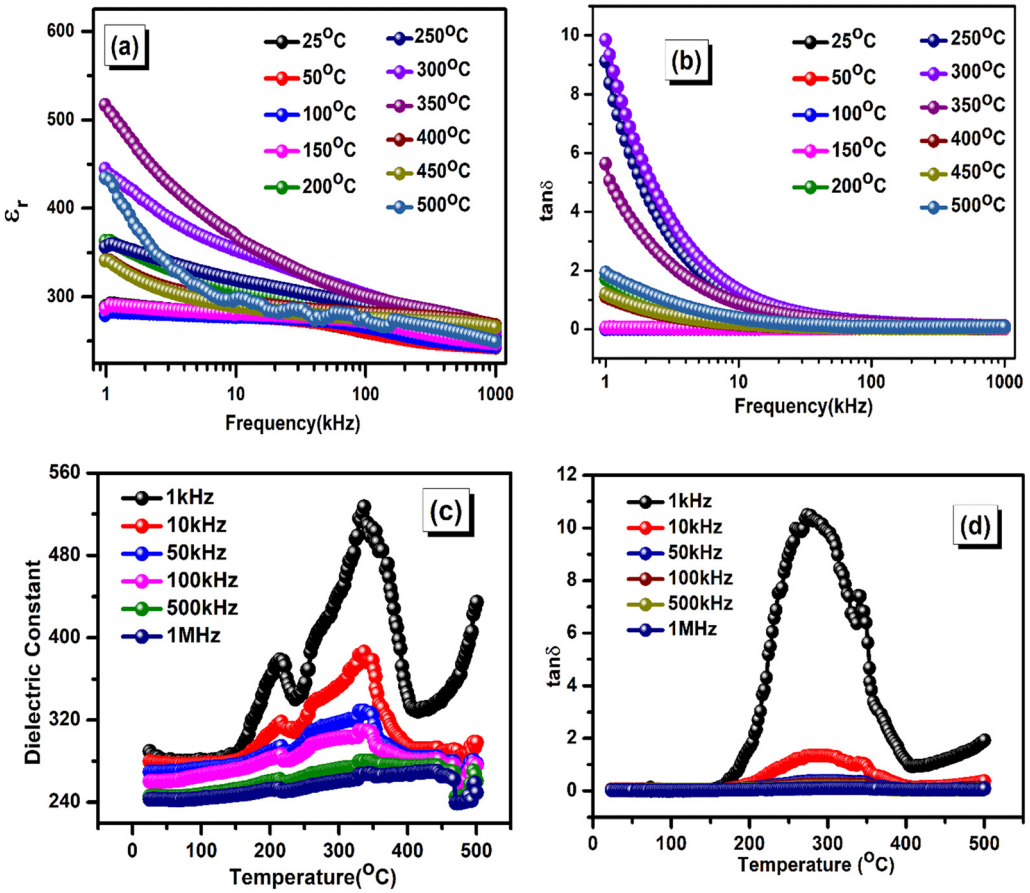

Fig. 5 (a) and (b) Variation of the dielectric constant and tangent loss *versus* frequency. (c) and (d) Variation of the dielectric constant and tangent loss *versus* temperature of $BiFeWO_6$.

atomic, dipolar, and interfacial. Space charges are the polarizable units for interfacial polarization. With a field frequency below 1 kHz, the interfacial polarization persists. This is the reason for the high dielectric constant value in lower-frequency regions. Around 1 kHz, dipolar polarization comes into the picture, which results in the lowering of the dielectric constant values at all studied temperatures, as depicted in the plot. Atomic/ionic polarization occurs at around 30–40 kHz, as the increase in magnitude pulls the center of the negatively charged electron cloud away from the nucleus. This further reduces the value of the dielectric constant. All other polarization ceases at a frequency higher than 100 kHz, resulting in electronic polarization dominating the polarization phenomenon. Thus, at higher frequencies, the dielectric constant contribution of the material is solely due to the electronic polarization, which can be understood from the merged plots for all temperatures. At low frequencies, the entire dielectric constant value is due to space polarization. As the frequency exceeds a certain value, dipoles lose their ability to align according to the applied field. The contributions of other polarization units decrease, leaving behind only electronic polarization. Thus, the dielectric constant values become invariant and the distinct plots merge at higher frequency regions.[57–59] The loss factor $\tan\delta$ arises due to the phase difference resulting from energy loss during the polarization phenomena at various frequencies. The tangent loss appears in a material if the polarization cannot follow with the applied electric field. The difference in energy occurs because the total polarization lags behind the applied field. As shown in plot 5(b), the tangent loss value is high at lower frequency regions due to the higher values of the dielectric constant. As the frequency increases, the value lowers. The dielectric loss value becomes minimum and invariant as the loss at higher frequencies is only due to electronic polarization, following the same pattern as that for the dielectric constant. The above phenomena were explained by Maxwell–Wagner's two-layer model and Koop's theory.[47] While considering electrical conduction, electrons are more active at grain boundaries in low frequencies whereas at grains during high frequencies. The grain boundaries are characterized by high resistance; hence, there is more electrical energy loss to facilitate carrier motion when the frequency of the applied field is low. In contrast, grains offer relatively low resistance; as a result, energy loss is minimized as the applied field frequency increases. Debye's relaxation model also explains the decrease of the dielectric constant, as well as the loss value with an increase in the applied field frequency. Since conductivity is frequency-dependent, the accumulation of charge carriers at grain boundaries leads to interfacial or space-charge polarization.[58]

The variation plot of the dielectric constant and tangent loss in a temperature range of 25 °C to 500 °C at a frequency range of 1 kHz–1 MHz is depicted in Fig. 5(c and d). The dielectric constant increases with rising temperature, but decreases as the frequency increases. At lower temperatures, the dipoles lack sufficient energy to align with the applied electric field, resulting in a lower dielectric constant.[59] In Fig. 5(c), around the reported Néel's temperature (~370 °C), an anomaly can be observed in the permittivity value.[60] The peaks of the dielectric constant value are due to the change in state of the electric dipole ordering, which is probably due to the presence of an anti-ferromagnetic transition or magnetoelectric effect in the sample.[61] The Landau–Devonshire theory of phase transition describes such an anomaly in magnetoelectric systems, which is an effect of vanishing magnetic order on electric order.[62] The plot corresponding to 1 kHz frequency shows the maximum value of the dielectric constant at around 350 °C. As the frequency increases, the ε_{max} value decreases due to the electron–phonon interactions.[63] Above 390 °C, the increase in the value of the dielectric constant can be attributed to the thermally activated transport process and the presence of space charges. The space charge contribution is the result of oxygen vacancies created during the sintering of sample pellets at high temperatures.[64] Due to the oxygen vacancies, the valency state of Fe^{3+} changes to Fe^{2+}. Besides the oxygen vacancies, the rise in ε_r value also affects the electron hopping in the direction of the applied electric field between the Fe^{3+} and Fe^{2+} octahedral sites.[65] Above 390 °C, an increase in the value of ε_r can be seen, which is due to the dipolar contribution of the $BiFeO_3$ ferroelectric component. Fig. 5(d) shows the temperature dependence of tanδ in a frequency range of 1 kHz to 1 MHz. The plots follow a similar pattern as that of ε_r. In low-temperature regions, the plots are merged into one. However, with an increase in temperature, the tanδ value increases rapidly following an increase in ε_r values. For temperature values above 300 °C, the values decrease due to the scattering of thermally activated charge carriers and the oxygen point defects. For an ideal case, the material should possess high resistance and low dielectric loss. The vacancies generated during high-temperature sintering may lead to the release of single or double-ionized oxygen vacancies, accompanied by the liberation of one or two electrons, respectively. Dielectric relaxation is influenced by dipoles, while oxygen vacancies extend beyond a single unit cell, impacting the entire material and contributing to an increase in ionic conductivity.

3.7. Impedance study

Impedance spectroscopy is related to the permittivity and distinguishes between the conducting and non-conducting regions of the sample. At shorter time scales, electrical spectroscopy serves as an effective tool for analyzing both electronic and ionic conduction properties. The frequency-dependent permittivity spectrum can be measured from these relaxation times. Permittivity reduces the dielectric constant.[66]

Mathematical tools used in electrical impedance spectroscopy are as follows:

$$Z^{*} = Z' + jZ''$$

$$Z' = \frac{R}{1 + (\omega\tau)^2}$$

$$Z'' = \frac{-\omega R\tau}{1 + (\omega\tau)^2}$$

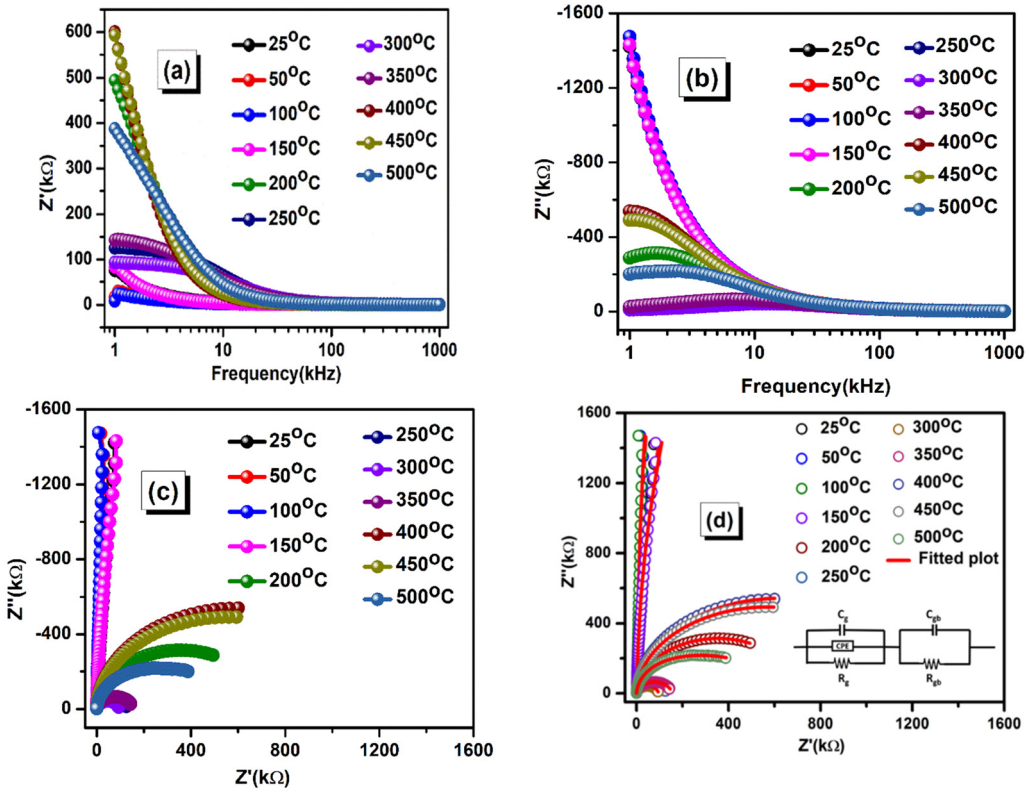

Fig. 6 (a) Z' *versus* frequency, (b) Z'' *vs.* frequency and (c) Nyquist plots. (d) Fitted Nyquist plots of $BiFeWO_6$.

where Z^* represents the complex impedance, with Z' as its real part and Z'' as its imaginary part; R denotes resistance and j is the imaginary unit $\sqrt{-1}$, while ω and τ correspond to the angular frequency and relaxation time, respectively.[67] Fig. 6(a and b) shows the frequency dependence plots of the Z' and Z'' complex impedances at selected temperatures. As can be seen from the plot, the values of both Z' and Z'' decrease with the increase in frequency and temperature. The Z' plots at higher frequencies merge, owing to the release of space charges, resulting in a reduction of barrier properties in the sample at higher frequencies.[67]

The increase in conductivity observed in the sample with rising temperature and frequency is associated with a single relaxation phenomenon. This tells us about the negative temperature coefficient of the resistance behaviour of the sample. The negative temperature coefficient of resistance (NTCR) behaviour is a defining characteristic of semiconducting materials, indicating the dielectric nature of the sample.[68] The spectrum loss of Z'' in Fig. 6(b) varies with frequency, as evidenced by the presence of a distinct peak. The shift of the relaxation process to higher frequency regions with increasing temperature indicates its temperature dependence. The asymmetrically broadened peaks observed over time suggest the presence of multiple relaxation mechanisms. At lower temperatures, the relaxation is primarily influenced by electrons and immobile ions. Conversely, at higher temperatures, oxygen vacancies and defects play a dominant role. The conductivity in the sample arises from electron hopping and oxygen vacancies generated during high-temperature sintering of the pellets, facilitating charge transport among localized sites. Fig. 6(c and d) illustrates the Nyquist plots and fitted Nyquist plots of the sample at some selected temperatures, offering insights into the roles of grains and grain boundaries in its conduction mechanism. At lower frequencies, conduction is primarily governed by grain boundaries. In contrast, at higher temperatures, grains play a dominant role. The presence of semicircular arcs in the Nyquist plot further confirms the semiconducting nature of the sample. This equivalent circuit is composed of a suitable combination of resistance (R) and capacitance (C) connected in parallel for each arc. In addition, a constant phase element (Q) is coupled with the RC circuit, providing information about the depression angle, *i.e.*, a departure from ideal Debye-type relaxation behavior. To provide a detailed view of the actual contribution of the grain and grain boundary, the Nyquist data were fitted and simulated with an equivalent electrical circuit, *i.e.*, (CQR)(CR) at some selected temperatures. In this study, the fitted parameters obtained from fitting the Nyquist data using the ZSIMPWIN version 2.0 software code are bulk (grain) capacitance (C_g), constant phase factor (Q), bulk resistance (R_g), grain boundary resistance (R_{gb}), capacitance (C_{gb}) and frequency power (n), and these are listed in Table 1. It is observed that the grain boundary effect is suppressed and grain resistance becomes effective at higher temperatures. The resistance at the grain boundary decreases from $8.943 \times 10^9\ \Omega\ cm^2$ at 25 °C to $3.547 \times 10^5\ \Omega\ cm^2$ at 500 °C. This confirms the NTCR character of the studied sample.[69]

Table 1 Fitting parameters for $BiFeWO_6$ from Nyquist plots after coupling with the equivalent circuit (CQR)(CR) using ZSIMPWIN version 20

Temperature	C_g (F cm^{-2})	Q (S-s^2 cm^{-2})	R_g (Ω cm^2)	Frequency exponent (n)	R_{gb} (Ω cm^2)	C_{gb} (F cm^{-2})
25 °C	4.9×10^{-10} (Expt.)	2.714×10^{-10} (Expt.)	8.943×10^{9} (Expt.)	21.06	2.388×10^{7} (Expt.)	1.122×10^{-10} (Expt.)
	4.9×10^{-10} (Fitting)	2.717×10^{-6} (Fitting)	1.878×10^{16} (Fitting)		2.387×10^{7} (Fitting)	1.122×10^{-10} (Fitting)
50 °C	6.205×10^{-10} (Expt.)	0.002798 (Expt.)	1.427×10^{10} (Expt.)	39.46	6.174×10^{7} (Expt.)	1.089×10^{-10} (Expt.)
	6.205×10^{-10} (Fitting)	2.8×10^{-5} (Fitting)	3.741×10^{11} (Fitting)		6.172×10^{7} (Fitting)	1.089×10^{-10} (Fitting)
100 °C	6.411×10^{-10} (Expt.)	5.22×10^{-5} (Expt.)	1.048×10^{11} (Expt.)	59.03	6.739×10^{7} (Expt.)	1.084×10^{-10} (Expt.)
	6.412×10^{-10} (Fitting)	5.221×10^{-5} (Fitting)	7.163×10^{11} (Fitting)		6.737×10^{7} (Fitting)	1.084×10^{-10} (Fitting)
150 °C	4.972×10^{-10} (Expt.)	4.842×10^{-8} (Expt.)	1.527×10^{11} (Expt.)	30.48	1.986×10^{7} (Expt.)	1.11×10^{-10} (Expt.)
	4.972×10^{-10} (Fitting)	4.842×10^{-6} (Fitting)	3.523×10^{15} (Fitting)		1.986×10^{7} (Fitting)	1.11×10^{-10} (Fitting)
200 °C	2.975×10^{-19} (Expt.)	2.949×10^{-10} (Expt.)	6.017×10^{5} (Expt.)	1.356	1.012×10^{5} (Expt.)	4.621×10^{-10} (Expt.)
	2.975×10^{-19} (Fitting)	2.95×10^{-10} (Fitting)	6.016×10^{5} (Fitting)		1.012×10^{5} (Fitting)	4.621×10^{-10} (Fitting)
250 °C	7.706×10^{-11} (Expt.)	1.843×10^{-9} (Expt.)	1.285×10^{5} (Expt.)	1.108	236.7 (Expt.)	1.633×10^{-9} (Expt.)
	7.706×10^{-11} (Fitting)	1.843×10^{-10} (Fitting)	1.285×10^{5} (Fitting)		236.8 (Fitting)	1.633×10^{-9} (Fitting)
300 °C	7.226×10^{-11} (Expt.)	4.043×10^{-10} (Expt.)	9.554×10^{4} (Expt.)	9.018	107.1 (Expt.)	4.174×10^{-9} (Expt.)
	7.24×10^{-11} (Fitting)	4.051×10^{-10} (Fitting)	9.554×10^{4} (Fitting)		107.1 (Fitting)	4.131×10^{-9} (Fitting)
350 °C	8.682×10^{-11} (Expt.)	7.508×10^{-10} (Expt.)	1.414×10^{5} (Expt.)	1.746	1.413×10^{4} (Expt.)	6.576×10^{-10} (Expt.)
	8.684×10^{-11} (Fitting)	7.515×10^{-10} (Fitting)	1.414×10^{5} (Fitting)		1.413×10^{4} (Fitting)	6.577×10^{-10} (Fitting)
400 °C	4.821×10^{-14} (Expt.)	2.835×10^{-11} (Expt.)	9.344×10^{5} (Expt.)	2.83	2.799×10^{5} (Expt.)	2.744×10^{-10} (Expt.)
	1.528×10^{-16} (Fitting)	2.835×10^{-10} (Fitting)	9.344×10^{5} (Fitting)		2.798×10^{5} (Fitting)	2.744×10^{-10} (Fitting)
450 °C	8.318×10^{-19} (Expt.)	2.573×10^{-10} (Expt.)	3.926×10^{5} (Expt.)	2.461	6.974×10^{5} (Expt.)	2.741×10^{-10} (Expt.)
	8.307×10^{-19} (Fitting)	2.576×10^{-10} (Fitting)	3.921×10^{5} (Fitting)		6.978×10^{5} (Fitting))	2.738×10^{-10} (Fitting)
500 °C	2.64×10^{-18} (Expt.)	1.088×10^{-8} (Expt.)	3.547×10^{5} (Expt.)	2.78	2.292×10^{5} (Expt.)	1.663×10^{-10} (Expt.)
	2.419×10^{-18} (Fitting)	1.088×10^{-9} (Fitting)	3.547×10^{5} (Fitting)		2.292×10^{5} (Fitting)	1.663×10^{-10} (Fitting)

3.8. Modulus study

Different phenomena, *e.g.*, bulk properties, conduction effect, relaxation time, effect of grain boundaries, electrode polarization, and electric transport process, can be understood from the electric modulus spectroscopy. It also helps in separating spectral components having different capacitances but the same resistances. Mathematical tools that were useful in calculating the complex modulus (M^*), real modulus (M') and complex modulus (M'') are as follows:

$$M^* = M' + jM'',$$

$$M' = B\frac{(\omega\tau)^2}{1+(\omega\tau)^2},$$

and

$$M'' = B\frac{\omega\tau}{1+(\omega\tau)^2}$$

where, $j = (-1)^{1/2}$; τ = relaxation time and ω = angular frequency. The bulk and grain boundary effects, along with the inhomogeneous nature of the polycrystalline sample, can be analyzed using the equations, which could not be fully explored through impedance spectroscopy. Additionally, modulation formulations play a crucial role in suppressing electrode effects, ensuring a more accurate characterization of the sample's electrical properties.[70] Fig. 7(a) represents the frequency *versus* real modulus (M') graph in a frequency range of 1 kHz–1 MHz at some selected temperatures. The 25 °C–150 °C plots show that at the low-frequency regions, the M' values are at their peak values compared to the rest of the temperature plots. The plots for 250 °C–350 °C have modulus values that are nearly equal to zero in the low-frequency regions. In the low-frequency regions, the modulus value dropping to zero may be due to the absence of electrode polarization or a low value. The merging of the plots and the attainment of high M' values in higher frequency regions can be attributed to low-mobility charge carriers, coupled with the absence of a restoring force under the induced electric field.[70] The M'' value as a function of frequency for the selected temperatures is plotted in Fig. 7(b). The M'' values increase with the increase in frequencies and reach a maximum value of M''_{max}. The peaks for M''_{max} shift towards a higher frequency region, depicting the presence of a relaxation phenomenon occurring in the sample.[71] The capacitance is inversely proportional to the height of the peak. The plots illustrate the transition from long-range to short-range charge carrier mobility. The region to the left of the peaks corresponds to long-range mobile charge carriers. Meanwhile, beyond M''_{max}, the ions become confined within potential wells due to the short-range mobility of the charge carriers. A study of M'' confirms the occurrence of non-Debye relaxation behaviour concluded from the appearance of asymmetrically broadened peak curves, unlike in an ideal Debye type.

The appearance of arcs at a frequency in the Cole–Cole plots shown in Fig. 7(c) signifies that the sample material has a single phase. The change in the nature of the curves with a temperature change is due to a change in the capacitances,

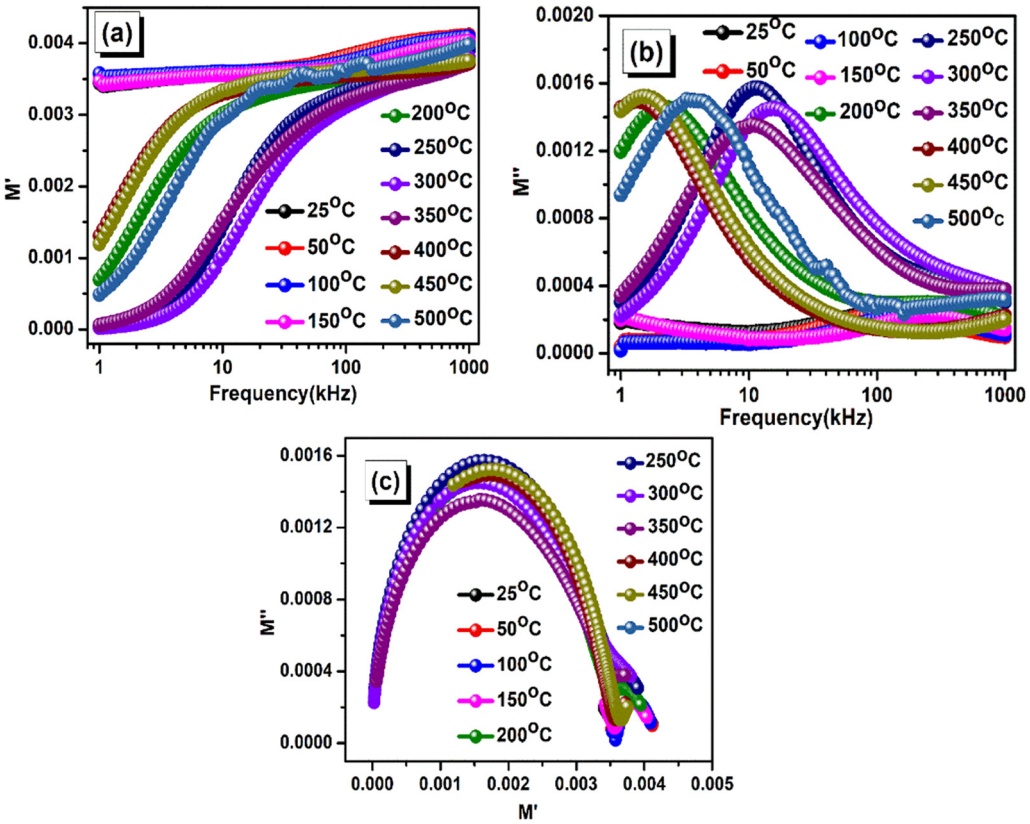

Fig. 7 (a) *M′ versus* frequency, (b) *M″ versus* frequency, and (c) Cole–Cole plots of $BiFeWO_6$.

which tells us about the temperature dependence of the capacitance. Some curves in the Cole–Cole plots have their centres lying below the real modulus axis, again providing evidence of the presence of a non-Debye-type relaxation process in the material. The intercept of large curves on the real modulus axis gives the value of the capacitance contribution from grains, whereas the intercepts of the smaller curves give the grain boundary capacitance contribution. These semicircular arcs are also an indication of the semiconducting nature of the sample.[72]

3.9. AC conductivity study

The ac conductivity of a sample can be calculated from dielectric data using the relation: $\sigma_{ac} = \omega\varepsilon_r\varepsilon_0\tan\delta$, where ω is the angular frequency, ε_0 is the permittivity of free space (approximately 8.854×10^{-12} F m^{-1}), ε_r is the relative permittivity (or dielectric constant), and $\tan\delta$ is the dielectric loss.[73] At low frequencies, the frequency-dependent conductivity plot stabilizes, forming a plateau that signifies DC conductivity, resulting from the random dispersion of ionic charge carriers through active hopping. On the other hand, in the high-frequency region, the plot becomes dispersive due to an increase in the conductivity. This increase in conductivity at high frequencies is indicative of the dynamic nature of charge transfer processes in the material. In essence, these studies allow us to understand the complex interplay between charge carriers, their transfer processes, and how these factors influence the overall conductivity of the material. The frequency dependence of the conductivity of a sample can indeed be studied using Jonscher's universal power law, which is given by the equation: $\sigma_{ac} = \sigma_{dc} + A\omega^n$, where σ_{ac} is the ac conductivity, σ_{dc} is the dc conductivity, A is the polarizability strength, ω is the angular frequency, and n is the frequency exponent which ranges from 0 to 2.[74]

The fitting data are recorded in Table 2. This law is widely used in the study of dielectric materials, and provides valuable insights into the behaviour of charge carriers in the material. The parameters A and n are typically determined through experimental measurements, and can provide information about the material's response to different frequencies.

Table 2 Evaluated values of the σ_{dc}, n, A, and R^2 of $BiFeWO_6$

Temperature (°C)	σ_{dc} (S m^{-1})	n	A	R^2
25	-1.0715×10^{-5}	0.7778	1.10156×10^{-8}	0.84933
50	-1.3135×10^{-5}	0.77356	1.16045×10^{-8}	0.80118
100	-1.8911×10^{-5}	0.77889	1.27098×10^{-8}	0.82463
150	-1.1215×10^{-5}	0.76152	1.50523×10^{-8}	0.98018
200	2.6256×10^{-5}	0.80084	1.21889×10^{-8}	0.99083
250	1.6592×10^{-4}	0.81095	1.35699×10^{-8}	0.99628
300	2.3386×10^{-4}	0.81115	1.65958×10^{-8}	0.99929
350	1.6835×10^{-4}	0.97778	1.77533×10^{-9}	0.99788
400	2.6881×10^{-5}	1.42847	2.2962×10^{-12}	0.9996
450	3.0873×10^{-5}	1.46646	1.1702×10^{-12}	0.9988
500	4.9793×10^{-5}	1.11066	2.3723×10^{-10}	0.9979

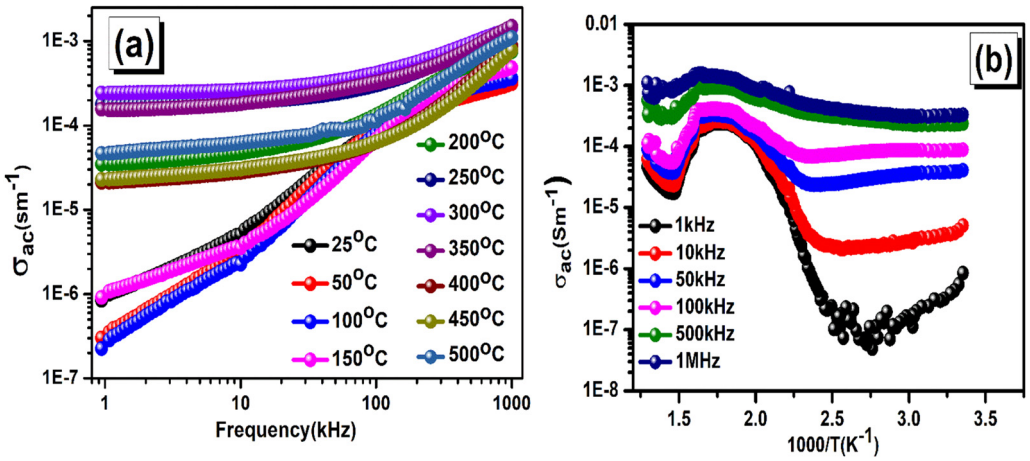

Fig. 8 (a) σ_{ac} *versus* frequency and (b) σ_{ac} *versus* 1000/T plots of $BiFeWO_6$.

Fig. 8(a and b) illustrates the variation of the AC conductivity as a function of frequency and $10^3/T$ (K^{-1}) at some selected frequencies. As shown in Fig. 8(a), the AC conductivity increases with both frequency and temperature, where the lower portion of the conductivity plot contributes to the DC conductivity. Examining the temperature dependence of the AC conductivity provides insights into the total real charge carriers within the sample. The rise in AC conductivity with increasing temperature confirms the NTCR characteristic, indicating semiconducting behavior. The activation energy of the ceramic compound can be determined using the Arrhenius equation: $\sigma = \sigma_0 \times e^{\frac{-E_a}{k_B T}}$, where k_B represents the Boltzmann constant and E_a denotes the activation energy.[74] The computed activation energy values at different frequencies are presented in Table 3. The observed decrease in activation energy with increasing frequency supports the presence of a thermally activated relaxation mechanism in the sample.

3.10. Thermistor characteristics

In previous sections, we explored the dielectric, optical, conducting, and transport properties of the ceramic sample. The impedance characteristics show the presence of both grain and grain boundary effects, as well as its NTCR behaviour. With the interest of exploring the industrial application, the authors then studied the thermistor characteristics of the ceramic sample. There are two types of thermistors: positive temperature coefficient (PTC) and negative temperature coefficient NTC. In PTC thermistors, the resistance increases with the rise in temperature. Meanwhile, in NTC thermistors, the resistance decreases with the rise in temperature. Fig. 9(a) illustrates the variation of the resistance with temperature. The decrease in resistance with increasing temperature confirms the presence of the NTC thermistor nature up to 375 °C, PTC thermistor up to 425 °C, and then the NTC thermistor again up to 500 °C. Consequently, the $BiFeWO_6$ ceramic emerges as a promising candidate of a non-toxic thermistor suitable for various industrial applications.

Table 3 Evaluated values of the activation energy and corresponding frequency of $BiFeWO_6$

SI No.	Frequency	Activation energy (E_a) (meV)
1	1 kHz	374.81
2	10 kHz	291.69
3	50 kHz	188.28
4	100 kHz	135.63
5	500 kHz	66.47
6	1 MHz	49.17

(a) Activation energy

Fig. 9(b) illustrates the variations in the temperature-dependent activation energy (E_a). The activation energy is determined using the mathematical relation presented as: $E_a = k_B \times \beta$, where k_B denotes the Boltzmann constant and β represents the thermistor constant. The activation energy curve exhibits a similar trend when compared to the behavior of the thermistor constant.

(b) Thermistor constant (β)

Fig. 9(c) shows the variation of the thermistor constant with temperature. The thermistor constant can be calculated using the empirical relation: $\beta = \ln\left(\frac{R_1}{R_2}\right) / \ln\left(\frac{1}{T_1} - \frac{1}{T_2}\right)$, where R_1 and R_2 are the initial and final resistances at temperatures T_1 and T_2, respectively. The value of the thermistor constant falls in the good range for NTC thermistor applications.[75]

(c) Sensitivity factor (α)

Fig. 9(d) shows the variation of the sensitivity factor *versus* temperature. The sensitivity factor represents a crucial parameter of thermistors, quantifying the rate at which resistance varies in response to temperature fluctuations. The sensitivity factor is calculated using the following mathematical relation: $\alpha = \left(\frac{-\beta}{T^2}\right) \times 100$, where α is the sensitivity factor, β is the thermistor constant and T is the temperature in K.[75]

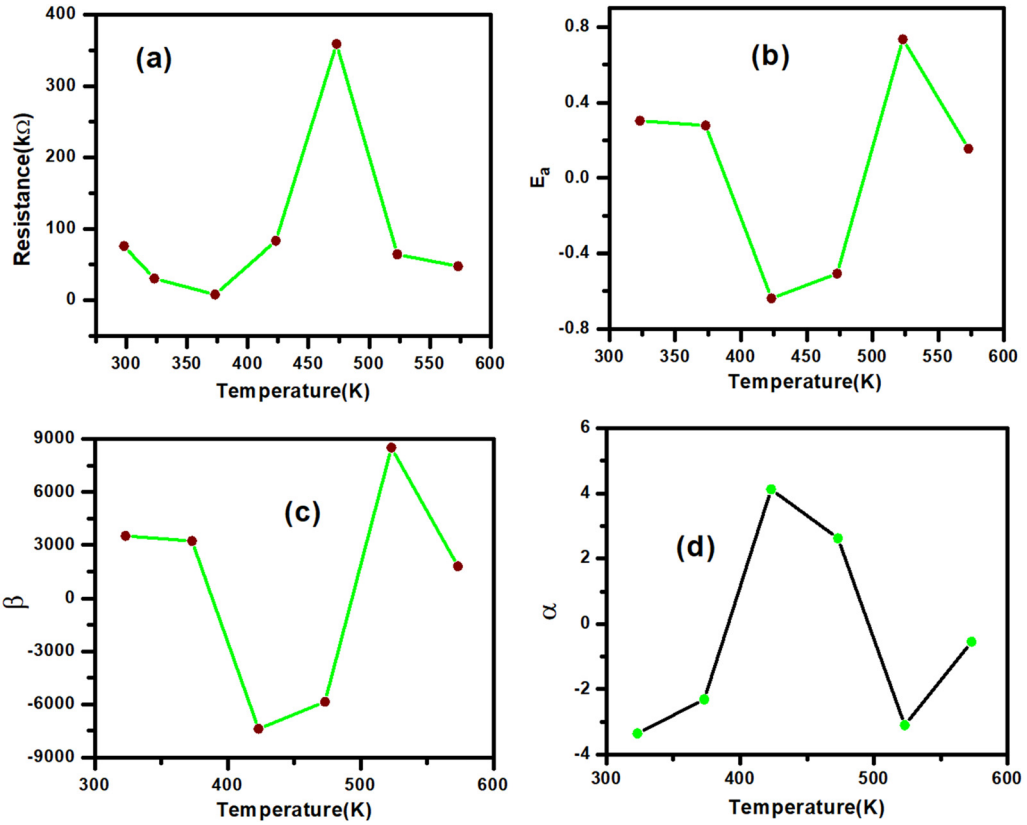

Fig. 9 (a) Variation in resistance with temperature, (b) activation energy *versus* temperature, (c) thermistor constant *versus* temperature and (d) sensitivity factor *versus* temperature of $BiFeWO_6$.

The mathematical relationship reveals that the parameter α exhibits direct proportionality to β, while demonstrating an inverse dependence on the square of the temperature. A higher α value corresponds to increased mobility of charge carriers compared to lower α magnitudes. The figure illustrates the variation of the sensitivity factor with temperature, highlighting its nonlinear inverse correlation with the square of the absolute temperature. The presence of half-filled transition metal cations at the B-site, forming an octahedral coordination with oxygen, plays a pivotal role in enhancing the material properties. This structural configuration significantly contributes to improved findings, thereby broadening the scope of thermistor-related applications.[76]

3.11. Ferroelectric properties

The *P–E* loop (Polarization–Electric field) is a graphical representation of the hysteresis behaviour of ferroelectric materials. It plots the polarization (P) against the electric field (E) applied to a material, demonstrating how the material retains its polarization even after the external field is removed. *P–E* loops are widely used in research and applications such as ferroelectric memory devices, capacitors, and sensors. Since we are working with ferroelectric materials, analyzing the *P–E* loop can provide valuable insights into their electrical properties. Lead-free relaxor ferroelectrics exhibit advantageous properties, including low remanent polarization, high maximum polarization, enhanced breakdown strength, and excellent thermal stability. Extensive research has been conducted on dielectric energy storage materials utilizing relaxor ferroelectrics, particularly those based on $SrTiO_3$ (ST), $BaTiO_3$ (BT), $NaNbO_3$ (NN), and $Na_{0.5}Bi_{0.5}TiO_3$ (NBT) ceramics.[77]

Fig. 10 shows the PE loops at three different temperatures of 25 °C, 50 °C, and 100 °C. The plot shows the maximum polarisation values of 0.024 μC cm^{-2} at 25 °C, which gradually decreases to 0.013 μC cm^{-2} at 50 °C and 0.005 μC cm^{-2} at 100 °C. Also, it can be observed that with an increase in temperature values, the values of the remnant polarisation and coercive field decrease.

The decrease in the coercive field value with increasing temperature while maintaining constant frequency signifies a reduction in the material's ability to retain polarization under an applied electric field. This phenomenon is primarily attributed to the thermal activation of dipoles, which disrupts their alignment and facilitates easier polarization switching. Additionally, as the material approaches its Curie temperature, its ferroelectric properties weaken, leading to a significant drop in the coercive field. Reduced domain wall pinning at elevated temperatures further contributes to this effect, as defects and lattice distortions that typically hinder domain movement become less restrictive. Moreover, structural softening at higher temperatures lowers the energy barrier required for domain switching, making polarization reversal more efficient. These temperature-dependent variations in the coercive field are

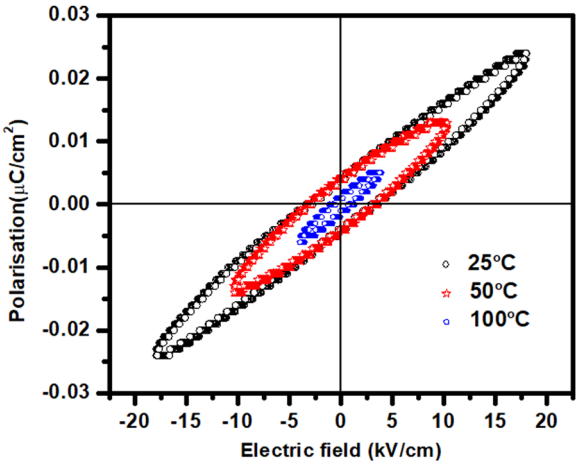

Fig. 10 *P–E* hysteresis loop of $BiFeWO_6$.

crucial for applications such as ferroelectric memory devices, capacitors, and sensors, where thermal stability plays a vital role in performance optimization.[78,79] An increase in temperature while keeping the frequency constant typically leads to a decrease in the remnant polarization. This occurs because the thermal energy disrupts the alignment of dipoles within the ferroelectric material, reducing its ability to retain polarization after the external electric field is removed. Additionally, as the temperature rises, the material may approach its Curie temperature, beyond which it loses its ferroelectric properties and transitions into a paraelectric phase. This phenomenon is crucial in applications such as pyroelectric sensors and ferroelectric memory devices, where temperature stability is essential.[80]

4. Conclusion

A $BiFeWO_6$ ceramic was prepared using a solid-state reaction method and crystallizes in a tetragonal structure. The sample has high density and purity, which is confirmed from SEM and EDX analysis. Raman spectrum analysis confirms the vibrational modes of all constituent elements in the $BiFeWO_6$ ceramic and supports the purity results from EDX analysis. The Raman study confirms the presence of all atomic vibrations. Meanwhile, the UV visible study reveals that the material has a bandgap energy of 1.41 eV, suitable for photovoltaic application. The dielectric study reveals the presence of the Maxwell-Wanger type of polarization effect, and possesses a high dielectric constant and low dielectric loss. The study of the impedance plots *versus* frequency at some selected temperatures confirms the NTCR nature, which is well-supported from the results of Nyquist plots. Analysis of the AC conductivity *versus* frequency & temperature reveals the fact that the conduction mechanism in the sample is controlled by the thermally activated charge carriers. Again, the calculated values of the activation energy from the conductivity study supports the semiconducting nature. The modulus plots reveal the presence of a non-Debye type of relaxation mechanism in the studied sample. Meanwhile, the resistance *versus* temperature plots reveal both NTC and PTC thermistor characteristics. Finally, the P-E loop reveals the ferroelectric nature of the studied sample, emerging as a promising non-toxic thermistor for ferroelectric applications.

Conflicts of interest

The authors declare that there is no conflict of interest.

Data availability

Data will be made available from the authors upon reasonable request.

Acknowledgements

The authors would like to thank the host institute for XRD and SEM-EDX characterization of our sample.

References

1 H. Schmid, Multi-ferroic magnetoelectric, *Ferroelectric*, 1994, **162**, 317–338.
2 H. Schmid, On ferrotoroidics and electrotoroidic, magnetotoroidic and piezotoroidic effects, *Ferroelectric*, 2001, **252**, 41–50.
3 I. E. Dzyaloshinsk, Institute for Physical Problems, Academy of Sciences, ''On the magneto-electrical effect in antiferromagnets,'' Jetp, vol. 10, no. 3, pp. 628–629, 1959, [Online]. Available: **https://www.jetp.ac.ru/cgi-bin/dn/e_010_03_0628.pdf**.
4 W. Eerenstein, N. D. Mathur and J. F. Scott, Multiferroic and magnetoelectric materials, *Nature*, 2006, **442**(7104), 759–765, DOI: **10.1038/nature05023**.
5 G. A. Smolenskii and I. E. Chupis, Ferroelectromagnets, *Phys.-Usp.*, 1982, **25**(7), 415–448, DOI: **10.1070/PU1982v025n07ABEH004570**.
6 Lottermoser and D. Meier, A short history of multiferroics, 2020.
7 S. Ghosh, H. Shankar and P. Kar, Materials Advances Recent developments of lead-free halide double perovskites: a new superstar in the optoelectronic field, *Mater. Adv.*, 2022, **1**, 3742–3765, DOI: **10.1039/d2ma00071g**.
8 P. N. Ravi Shankar and A. Sundaresan, Synthesis, characterization and multiferroic properties of the doubly-ordered polar perovskite $NaLnNiWO_6$ (Ln = Er, Tm, and Lu), *J. Magn. Magn. Mater.*, 2021, **540**, 168412, DOI: **10.1016/j.jmmm.2021.168412**.
9 H. A. Evans, L. Mao, R. Seshadri and A. K. Cheetham, Layered Double Perovskites, *Annu. Rev. Mater. Res.*, 2021, **51**, 351–380, DOI: **10.1146/annurev-matsci-092320-102133**.
10 L. Boudad, M. Taibi, A. Belayachi and M. Abd-Lefdil, Structural, morphological, dielectric and optical properties of

double perovskites $RBaFeTiO_6$(R = La, Eu), *RSC Adv.*, 2021, **11**(63), 40205–40215, DOI: 10.1039/d1ra06793a.

11 R. Das and R. N. P. Choudhary, Studies of electrical, magnetic and leakage-current characteristics of double perovskite: Dy_2CoMnO_6, *J. Alloys Compd.*, 2021, **853**, 157240, DOI: 10.1016/j.jallcom.2020.157240.

12 L. Chen, J. Ding and X. Zhu, A review on research progress of double perovskite oxides for oxygen evolution reaction electrocatalysts and supercapacitors, *RSC Appl. Interfaces*, 2025, vol. 2, 320–351, DOI: 10.1039/d4lf00395k.

13 J. B. Neaton, C. Ederer, U. V. Waghmare, N. A. Spaldin and K. M. Rabe, First-principles study of spontaneous polarization in multiferroic $BiFeO_3$, *Phys. Rev. B*, 2005, **71**(1), 14113, DOI: 10.1103/PhysRevB.71.014113.

14 B. B. Van Aken, T. T. M. Palstra, A. Filippetti and N. A. Spaldin, The origin of ferroelectricity in magnetoelectric $YMnO_3$, *Nat. Mater.*, 2004, **3**(3), 164–170, DOI: 10.1038/nmat1080.

15 M. Fiebig, Revival of the magnetoelectric effect, *J. Phys. D:Appl. Phys.*, 2005, **38**, R123–R152, DOI: 10.1088/0022-3727/38/8/R01.

16 A. Manbachi and R. S. C. Cobbold, Review Development and application of piezoelectric materials for ultrasound generation and detection, *Ultrasound*, 2011, 187–196.

17 A. S. Borovik-romanov, Piezomagnetism in the antiferromagnetic fluorides of cobalt and manganese, 2015.

18 I. Dzyaloshinsky, A thermodynamic theory of 'weak' ferromagnetism of antiferromagnetics, *J. Phys. Chem. Solids*, 1958, **4**(4), 241–255.

19 S.-W. C. Shuai Dong Jun-Ming Liu and Z. Ren, Multiferroic materials and magnetoelectric physics: symmetry, entanglement, excitation, and topology, *Adv. Phys.*, 2015, **64**(5–6), 519–626.

20 W. Eerenstein, N. D. Mathur and J. F. Scott, Multiferroic and magnetoelectric materials, *Nature*, 2006, **442**(7104), 759–765.

21 T. Kimura, T. Goto, H. Shintani, K. Ishizaka, T. Arima and Y. Tokura, Magnetic control of ferroelectric polarization, *Nature*, 2003, **426**(6962), 55–58, DOI: 10.1038/nature02018.

22 K. Z. Rushchanskii, *et al.*, A multiferroic material to search for the permanent electric dipole moment of the electron, *Nat. Mater.*, 2010, **9**(8), 649–654, DOI: 10.1038/nmat2799.

23 H. Katsura, N. Nagaosa and A. V. Balatsky, Spin Current and Magnetoelectric Effect in Noncollinear Magnets, *Phys. Rev. Lett.*, 2005, **95**(5), 57205, DOI: 10.1103/PhysRevLett.95.057205.

24 H. Palneedi, V. Annapureddy, S. Priya and J. Ryu, Status and Perspectives of Multiferroic Magnetoelectric Composite Materials and Applications, *Actuators*, 2016, **5**, 9.

25 Z. F. R. K. F. Wang and J. M. Liu, Multiferroicity—The coupling between magnetic and polarization orders, no. Tadp 392227.

26 N. A. Spaldin and M. Fiebig, The Renaissance of Magnetoelectric Multiferroics, *Science*, 2005, **309**(5733), 391–392, DOI: 10.1126/science.1113357.

27 R. Palai, H. Schmid, J. F. Scott and R. S. Katiyar, Raman spectroscopy of single-domain multiferroic $BiFeO_3$, *Phys. Rev. B:Condens. Matter Mater. Phys.*, 2010, **81**(6), 64110, DOI: 10.1103/PhysRevB.81.064110.

28 J. Wang, *et al.*, Epitaxial BiFeO3 multiferroic thin film heterostructures, *Science*, 2003, **299**(5613), 1719–1722, DOI: 10.1126/science.1080615.

29 A. Puhan, B. Bhushan, A. K. Nayak and D. Rout, *BiFeO3-based multiferroic materials and their properties*, Elsevier Inc, 2021, ch. 12, DOI: 10.1016/B978-0-12-822352-9.00008-0.

30 K. N. Kumar, S. A. Sattar, G. V. A. Reddy, R. I. Jafri and R. Premkumar, Structural, optical, and electrochromic properties of RT and annealed sputtered tungsten trioxide – (WO_3) thin films for electrochromic applications by using the GLAD technique, *J. Mater. Sci. Mater. Electron.*, 2023, **34**(28), 1–11, DOI: 10.1007/s10854-023-11285-x.

31 P. M. Woodward, A. W. Sleight and T. Vogt, Ferroelectric Tungsten Trioxide, *IEEE J. Solid-State Circuits*, 1997, **131**, 9–17.

32 J. Rout, B. N. Parida, P. R. Das and R. N. P. Choudhary, Structural, dielectric, and electrical properties of BiFeWO6 ceramic, *J. Electron. Mater.*, 2014, **43**(3), 732–739, DOI: 10.1007/s11664-013-2923-2.

33 A. Malathi, P. Arunachalam, A. Nirmala Grace, J. Madhavan and A. M. Al-Mayouf, A robust visible-light driven $BiFeWO_6$/BiOI nanohybrid with efficient photocatalytic and photoelectrochemical performance, *Appl. Surf. Sci.*, 2017, **412**, 85–89, DOI: 10.1016/j.apsusc.2017.03.199.

34 C. Lu, Y. Yin and H. Zhou, Construction of oxygen vacancy enriched Bi_2MoO_6/$BiFeWO_6$ heterojunction for efficient degradation of organic pollutants, *J. Solid State Chem.*, 2022, **312**, 123210, DOI: 10.1016/j.jssc.2022.123210.

35 F. F. Alharbi, S. Aman and N. Ahmad, *et al.*, Rational design of a $BiFeWO_6$ nanostructure for supercapacitor applications, *J. Solid State Electrochem.*, 2022, **26**, 1251–1258, DOI: 10.1007/s10008-022-05154-6.

36 N. Raengthon, C. McCue and D. P. Cann, *J. Adv. Dielectr.*, 2016, **6**, 1650002.

37 A. K. Singh, Experimental Methodologies for the Characterization of Nanoparticles, *Engineered Nanoparticles Structure, Properties and Mechanisms of Toxicity*, 2016, pp. 125–170, DOI: 10.1016/b978-0-12-801406-6.00004-2.

38 A. B. J. Kharrat, N. Moutia, K. Khirouni and W. Boujelben, Investigation of electrical behavior and dielectric properties in polycrystalline $Pr_{0.8}Sr_{0.2}MnO_3$ manganite perovskite, *Mater. Res. Bull.*, 2018, **105**, 75–83.

39 S. Patel, A. Raulji, D. Patel, D. Panchal, M. Dalwadi and U. Upadhyay, A Review on 'Uv Visible Spectroscopy, *Int. J. Pharm. Res. Appl.*, 2022, **7**(5), 1144–1151.

40 A. Meher, A. Palai, N. Ranjan Panda, S. Prakash Pati and D. Sahu, Synthesis of zinc oxide/bismuth oxide nanocomposite photocatalyst for visible light-assisted degradation of synthetic dyes and antibacterial application, *Environ. Sci. Pollut. Res.*, 2025, **1**, 1–25, DOI: 10.1007/s11356-024-35804-3.

41 J. Tauc, R. Grigorovici and A. Vancu, Optical Properties and Electronic Structure of Amorphous Germanium, *Phys. Status Solidi*, 1966, **15**(2), 627–637, DOI: 10.1002/pssb.19660150224.

42 K. S. Usha, R. Sivakumar and C. Sanjeeviraja, Optical constants and dispersion energy parameters of NiO thin films prepared by radio frequency magnetron sputtering technique, *J. Appl. Phys.*, 2013, **114**(12), 123501, DOI: 10.1063/1.4821966.

43 Y. Wang, *et al.*, One-step hydrothermal synthesis of a novel 3D BiFeWOx/Bi2WO6 composite with superior visible-light photocatalytic activity, *Green Chem.*, 2018, **20**(13), 3014–3023, DOI: 10.1039/c7gc03731g.

44 C. Lu, W. Wu and H. Zhou, In situ fabrication of BiOBr/BiFeWO6 heterojunction with excellent photodegradation activity under visible light, *J. Solid State Chem.*, 2021, **303**, 122465, DOI: 10.1016/j.jssc.2021.122465.

45 A. Priya, *et al.*, Fabrication of visible-light active $BiFeWO_6$/ZnO nanocomposites with enhanced photocatalytic activity, *Colloids Surf., A*, 2020, **586**, 124294, DOI: 10.1016/j.colsurfa.2019.124294.

46 J. A. Khan and J. Ahmad, Double perovskite La_2CrMnO_6: synthesis, optical and transport properties Double perovskite La_2CrMnO_6: synthesis, optical and transport properties, *Mater. Res. Exp.*, 2019, 0–12.

47 B. S. Tripathy, R. N. P. Choudhary and S. K. Parida, A Double Perovskite $BiFeMoO_6$: Microstructural, Optical, Dielectric and Transport Properties, *SPIN*, 2023, **13**(03), 2350011, DOI: 10.1142/S201032472350011X.

48 S. K. Tripathy, Refractive indices of semiconductors from energy gaps, *Opt. Mater.*, 2015, **46**, 240–246, DOI: 10.1016/j.optmat.2015.04.026.

49 P. Mallick, Effect of solvent on the microstructure and optical band gap of ZnO nanoparticles, *Indian J. Pure Appl. Phys.*, 2017, **55**(3), 187–192.

50 S. Munir, S. M. Shah, H. Hussain and R. Ali Khan, Effect of carrier concentration on the optical band gap of TiO2 nanoparticles, *Mater. Des.*, 2016, **92**, 64–72, DOI: 10.1016/j.matdes.2015.12.022.

51 C. Huang, F. Wang, C. Wu, H. Huang and C. Yang, NiO-TZO diode transmittance Huang2013_Article_DevelopingHigh-transmittanceHe.pdf, pp. 1–8, 2013.

52 M. H. Mamat, *et al.*, Synthesis, structural and optical properties of mesostructured, X-doped NiO (x = Zn, Sn, Fe) nanoflake network films, *Mater. Res. Bull.*, 2020, **127**, 110860, DOI: 10.1016/j.materresbull.2020.110860.

53 G. Malik, J. Jaiswal, S. Mourya and R. Chandra, Optical and other physical properties of hydrophobic ZnO thin films prepared by dc magnetron sputtering at room temperature, *J. Appl. Phys.*, 2017, **122**(14), 143105, DOI: 10.1063/1.5007717.

54 C. Beekman, A. A. Reijnders, Y. S. Oh, S. W. Cheong and K. S. Burch, Raman study of the phonon symmetries in BiFeO3 single crystals, *Phys. Rev. B:Condens. Matter Mater. Phys.*, 2012, **86**, 020403, DOI: 10.1103/PhysRevB.86.020403.

55 C. Himcinschi, J. Rix, C. Röder, M. Rudolph, M.-M. Yang, D. Rafaja, J. Kortus and M. Alexe, Ferroelastic domain identification in $BiFeO_3$ crystals using Raman spectroscopy, *Sci. Rep.*, 2019, **9**, 379–387, DOI: 10.1038/s41598-018-36462-5.

56 J. Bielecki, P. Svedlindh, D. T. Tibebu, S. Cai, S.-G. Eriksson, L. Börjesson and C. S. Knee, Structural and magnetic properties of isovalently substituted multiferroic BiFeO3: Insights from Raman spectroscopy, *Phys. Rev. B:Condens. Matter Mater. Phys.*, 2012, **86**, 184422, DOI: 10.1103/PhysRevB.86.184422.

57 P. Keburis, J. Banys, A. Brilingas, J. Prapuolenis, A. Kholkin and M. E. V. Costa, Dielectric properties of relaxor ceramics BBN, *Ferroelectrics*, 2007, **353**(1), 149–153, DOI: 10.1080/00150190701368109.

58 N. Ranjan Panda, S. K. Sahu, A. Palai, T. Yadav, D. Behera and D. Sahu, Unraveling the synergistic effects in ZnO-MoS_2 nanocomposite leading to enhanced photocatalytic, antibacterial and dielectric characteristics, *Chem. Phys. Impact*, 2024, **8**, 100550, DOI: 10.1016/j.chphi.2024.100550.

59 D. Sahu and N. Ranjan Panda, Synthesis of novel nanocomposite of g-C_3N_4 coated ZnO–MoS_2 for energy storage and photocatalytic applications, *Chemosphere*, 2024, **350**, 141014, DOI: 10.1016/j.chemosphere.2023.141014.

60 K. B. R. Varma and K. V. R. Prasad, Structural and dielectric properties of Bi2NbxVi−xO5.5 ceramics, *J. Mater. Res.*, 1996, **11**(9), 2288–2292, DOI: 10.1557/JMR.1996.0291.

61 S. Mishra, R. N. P. Choudhary and S. K. Parida, Microstructure, dielectric relaxation, optical, and ferroelectric studies of a lead-free double perovskite: BaLiFeMoO6, *J. Korean Ceram. Soc.*, 2023, **60**, 310–330.

62 P. Fischer, M. Polomska, I. Sosnowska and M. Szymanski, Temperature dependence of the crystal and magnetic structures of BiFeO3, *J. Phys. C Solid State Phys.*, 1980, **13**(10), 1931–1940, DOI: 10.1088/0022-3719/13/10/012.

63 R. K. Mishra, D. K. Pradhan, R. N. P. Choudhary and A. Banerjee, Dipolar and magnetic ordering in Nd-modified BiFeO3 nanoceramics, *J. Magn. Magn. Mater.*, 2008, **320**(21), 2602–2607, DOI: 10.1016/j.jmmm.2008.05.005.

64 L. Benguigui, Thermodynamic theory of the morphotropic phase transition tetragonal-rhombohedral in the perovskite ferroelectrics, *Solid State Commun.*, 1972, **11**(6), 825–828, DOI: 10.1016/0038-1098(72)90280-3.

65 S. Mishra, R. N. P. Choudhary and S. K. Parida, Structural, Dielectric, Electrical and Optical Properties of Li/Fe Modified Barium Tungstate Double Perovskite for Electronic Devices, *Ceram. Int.*, 2022, **48**, 17020–17030.

66 R. J. D. Tilley, Correlation between dielectric constant and defect structure of non-stoichiometric solids, *Nature*, 1977, **269**(5625), 229–231, DOI: 10.1038/269229a0.

67 N. Singh, A. Agarwal, S. Sanghi and P. Singh, Synthesis, microstructure, dielectric and magnetic properties of Cu substituted Ni–Li ferrites, *J. Magn. Magn. Mater.*, 2011, **323**(5), 486–492, DOI: 10.1016/J.JMMM.2010.09.053.

68 S. Mishra, R. N. P. Choudhary and S. K. Parida, Structural, dielectric, electrical and optical properties of a double perovskite: BaNaFeWO6 for some device applications, *J. Mol. Struct.*, 2022, **1265**, 133353, DOI: 10.1016/J.MOLSTRUC.2022.133353.

69 S. K. Parida and R. N. P. Choudhary, Preparation method and cerium dopant effects on the properties of BaMnO3 single perovskite, *Phase Transitions*, 2020, **93**(10–11), 981–991, DOI: 10.1080/01411594.2020.1817451.

70 Z.-L. Hou, M.-S. Cao, J. Yuan, X.-Y. Fang and X.-L. Shi, High-temperature conductance loss dominated defect level in h-BN: Experiments and first-principles calculations, *J. Appl. Phys.*, 2009, **105**(7), 76103, DOI: **10.1063/1.3086388**.

71 W.-L. Song, M.-S. Cao, Z.-L. Hou, X.-Y. Fang, X.-L. Shi and J. Yuan, High dielectric loss and its monotonic dependence of conducting-dominated multiwalled carbon nanotubes/silica nanocomposite on temperature ranging from 373 to 873 K in X-band, *Appl. Phys. Lett.*, 2009, **94**(23), 233110, DOI: **10.1063/1.3152764**.

72 H. Singh, A. Kumar and K. L. Yadav, Structural, dielectric, magnetic, magnetodielectric and impedance spectroscopic studies of multiferroic BiFeO3–BaTiO3 ceramics, *Mater. Sci. Eng. B*, 2011, **176**(7), 540–547, DOI: **10.1016/j.mseb.2011.01.010**.

73 V. Provenzano, L. P. Boesch, V. Volterra, C. T. Moynihan and P. B. Macedo, Electrical Relaxation in $Na_2O_3SiO_2$ Glass, *J. Am. Ceram. Soc.*, 1972, **55**(10), 492–496, DOI: **10.1111/j.1151-2916.1972.tb13413.x**.

74 A. K. Jonscher, The 'universal' dielectric response, *Nature*, 1977, **267**(5613), 673–679, DOI: **10.1038/267673a0**.

75 S. Sahoo, Enhanced time response and temperature sensing behavior of thermistor using Zn-doped CaTiO3 nanoparticles, *J. Adv. Ceram.*, 2018, **7**, 99–108.

76 D. Saha, A. Das Sharma, A. Sen and H. S. Maiti, Preparation of bixbyite phase (MnxFe1–x)2O3 for NTC thermistor applications, *Mater. Lett.*, 2002, **55**, 403–406.

77 S. Zhang, B. Malič and J. F. Li, *et al.*, Lead-free ferroelectric materials: Prospective applications, *J. Mater. Res.*, 2021, **36**, 985–995, DOI: **10.1557/s43578-021-00180-y**.

78 W. C. Nunes, W. S. D. Folly, J. P. Sinnecker and M. A. Novak, Temperature dependence of the coercive field in single-domain particle systems, *Phys. Rev. B:Condens. Matter Mater. Phys.*, 2004, **70**, 014419, DOI: **10.1103/PhysRevB.70.014419**.

79 Y. Zhang, Z. Chen, W. Cao and Z. Zhang, Temperature and frequency dependence of the coercive field of $0.71PbMb_{1/3}Nb_{2/3}O_3$–$0.29PbTiO_3$ relaxor-based ferroelectric single crystal, *Appl. Phys. Lett.*, 2017, **111**, 172902, DOI: **10.1063/1.4998187)**.

80 H. Yu and C. Shin, Impact of Rapid-Thermal-Annealing Temperature on the Polarization Characteristics of a PZT-Based Ferroelectric Capacitor, *Electronics*, 2021, **10**(11), 1324, DOI: **10.3390/electronics10111324**.